Oceanologia 64 (2022) 131—144

Available online at www.sciencedirect.com

ScienceDirect

journal homepage: www.journals.elsevier.com/oceanologia

ORIGINAL RESEARCH ARTICLE

Response of the Bay of Bengal to super cyclone Amphan examined using synergistic satellite and in-situ observations

Neethu Chacko*, Chiranjivi Jayaram

Regional Remote Sensing Centre — East National Remote Sensing Centre, ISRO, Kolkata, India

Received 9 February 2021; accepted 30 September 2021
Available online 14 October 2021

KEYWORDS
Amphan;
Tropical cyclone;
Bay of Bengal;
Sea Surface Temperature;
Salinity;
Upper ocean response;
Mixed layer budget

Abstract Tropical cyclone Amphan is the first super cyclone that happened in the north Indian Ocean in the last 20 years. In this work, multi-platform datasets were used to investigate the responses of the upper ocean to cyclone Amphan. The most striking response was the cold wake left by the cyclone spanning the entire Bay of Bengal with an amplitude up to ~4°C. Satellite salinity observations revealed that the maximum increase in surface salinity was ~1.5 PSU on the right side of the track of Amphan. Surface circulation was also observed to be modulated with the passage of a cyclone with a rightward bias in the change in its speed and direction. The currents observed from a moored buoy showed strong inertial oscillations. Argo observations showed that changes induced by the cyclone occurred up to 150 m depth of the cyclone and ocean heat content in the upper 150 m depth decreased due to the passage of the cyclone. There was an enhancement of surface chlorophyll concentration (~1.5 mg/m^3) after the passage of the cyclone, which was centred along the track of the cyclone where the winds were the highest. Mixed layer heat and salinity budget analysis showed that the sea surface cooling and increase in salinity was primarily driven by vertical mixing processes, though horizontal advection contributed meagrely. This study also brings forward the fact that regional differences exist in the responses of the ocean to the forcing of cyclones.

* Corresponding author at: Regional Remote Sensing Centre — East National Remote Sensing Centre, ISRO, BG2, Action Area 1B, Kolkata, India.
E-mail address: neethuchacko@gmail.com (N. Chacko).
Peer review under the responsibility of the Institute of Oceanology of the Polish Academy of Sciences.

Production and hosting by Elsevier

https://doi.org/10.1016/j.oceano.2021.09.006

1. Introduction

Tropical cyclones are among the most devastating natural disasters that pose a significant threat to the property and lives of coastal regions around the world. The Bay of Bengal (BoB) experiences a greater number of cyclones annually compared to the Arabian Sea (Singh et al., 2000; Singh and Koll, 2020). BoB is prone to cyclones during pre-monsoon (March, April and May) and post-monsoon (October and November) seasons. A recent addition was the tropical cyclone Amphan, which happened in May 2020. Amphan was the first super-cyclone in the north Indian Ocean that happened after the super cyclone which occurred in the year 1999.

During the passage of a cyclone, the strong wind stress imposed by the cyclone produces various responses in the upper ocean. Cyclones induce intense mixing of ocean waters that results in entrainment and upwelling (Price, 1981). The upper ocean responds to strong cyclone forcing in many ways depending upon the strength, translation speed and the oceanic preconditions. The implications of these responses could be manifested in various physical and biological parameters such as sea surface temperature, salinity, chlorophyll concentration, and ocean currents. The most striking aspect of the oceanic response to cyclones is the modulation of the sea surface temperature (Cione and Uhlhorn, 2003; D'Asaro et al., 2007; Dare and McBride, 2011; Price et al., 1994; Schade and Emanuel, 1999) and upper ocean temperature structure (Maneesha et al., 2012). Stronger winds of the cyclones produce intense oceanic entrainment and upwelling, thereby deepening the mixed layer.

Sea surface salinity also undergoes variations under cyclones, which are also dependant on the underlying oceanic conditions (Lin et al., 2003; Sun et al., 2010; Sing and Koll, 2020). In addition to the cyclone induced vertical mixing of the near surface waters, precipitation due to cyclones also will have a profound impact on the ocean salinity. Cyclones also influence upper ocean biological processes, which result in phytoplankton blooms in the wake of the cyclone (Babin et al., 2004; Chacko, 2017; Chacko 2019; Chen et al., 2003; Jayaram et al., 2019; Walker et al., 2005). The strong cyclonic winds induce Ekman transport and subsequently initiate strong upwelling which brings cold nutrient-rich water towards the surface (Subrahmanyam et al., 2002). The interaction between the cyclone and the ocean is very complex and the response of the ocean is manifested in each parameter differently. For example, sea surface temperature cooling after a cyclone could vary from 1−9 degrees (Black and Dickey, 2008; Lin et al., 2003; Shang et al., 2001; Sun et al., 2010; Song et al., 2020). The changes induced by each cyclone are different and it is worthwhile to study the interactions and responses of the ocean to cyclones. It is also important to understand the variations of oceanic parameters and the environment itself with the cyclone locally.

Each tropical cyclone is unique in its genesis and the subsequent impact it leaves on the ocean that is also equally singular in nature. Ocean observations enable a detailed examination of the air-sea interaction processes associated with a cyclone. A synergistic utilization of satellite as well as in-situ data sets is thus imperative in understanding the changes induced by cyclones. In this study, satellite and in-situ observations were used to characterize the upper ocean response to super cyclone Amphan. The present study investigates the impact of super cyclone Amphan on the comprehensive response of the BoB in terms of sea surface winds, surface and subsurface variability of the temperature, salinity, currents, mixed layer depth, the heat and salt budgets, and chlorophyll concentration. We focus on the detailed processes and underlying dynamics for the rapid upper ocean response due to Amphan.

2. Material and methods

The six hourly cyclone track data and wind speeds used in this study were obtained from Regional Specialized Meteorological Centre (RSMC), India Meteorological Department (http://www.rsmcnewdelhi.imd.gov.in). To provide a basin-scale view of the upper ocean response to Amphan, we have analyzed gridded satellite data products. Daily Advanced Microwave Scanning Radiometer (AMSR-2) sea surface temperature and rainfall data used in this study were obtained from http://apdrc.soest.hawaii.edu/index.php. The product has a spatial resolution of 25 km x 25 km. Sea surface height anomalies (SSHA) are used to observe the signatures of mesoscale eddies. Daily SSHA data from Archiving, Validation, and Interpretation of Satellite Oceanographic (AVISO) data with a spatial resolution of 25 km x 25 km were used. The altimeter products were produced and distributed by AVISO (http://www.aviso.altimetry.fr/en/data/products/sea-surface-heightproducts/global/msla-h.html), as part of the Ssalto ground processing segment. Observations from a few in-situ platforms were analyzed to provide insights into the upper-ocean response to Amphan. The temperature and salinity observations from an Argo float (WMO ID: 2902230) located at the central Bay of Bengal were assessed. The Argo float was sampled at an interval of 5 days. The daily surface meteorological and oceanographic observations from a RAMA buoy (McPhaden et al., 2009) located at 90°E, 15°N were also used in this study. Observations from a moored buoy BD8 located at 89°E longitude and 18°N latitude was used in this study to characterize the variability of surface and subsurface temperature, salinity and currents. The moored buoy measures various parameters at 3 hourly intervals at various depths. The daily Soil Moisture Active Passive (SMAP) level 3, sea surface salinity data with a resolution of 0.33° x 0.33° were used to explore Amphan induced surface salinity variations. The daily wind data from Scatsat-1 with a spatial resolution of 0.25 degrees (Mandal et al., 2018) was used to assess the wind speeds during Amphan. The Visible Infrared Imaging Radiometer Suite (VIIRS) chlorophyll-*a* concentration at 4 km x 4 km at 8-day temporal scale was used in this study. VIIRS is one of the key instruments onboard the Suomi National Polar-Orbiting Partnership (Suomi NPP) spacecraft. The daily NCEP Climate Forecast System Version 2 (CFSV2) flux data products from Asia-Pacific Data Research Centre (APDRC) with a spatial resolution of 0.25 degrees were used in this study for the evaluation of mixed layer heat budget.

Mixed layer depth is defined as the depth at which the density increases by the amount which is equivalent to the decrease in temperature by 0.8°C from the surface

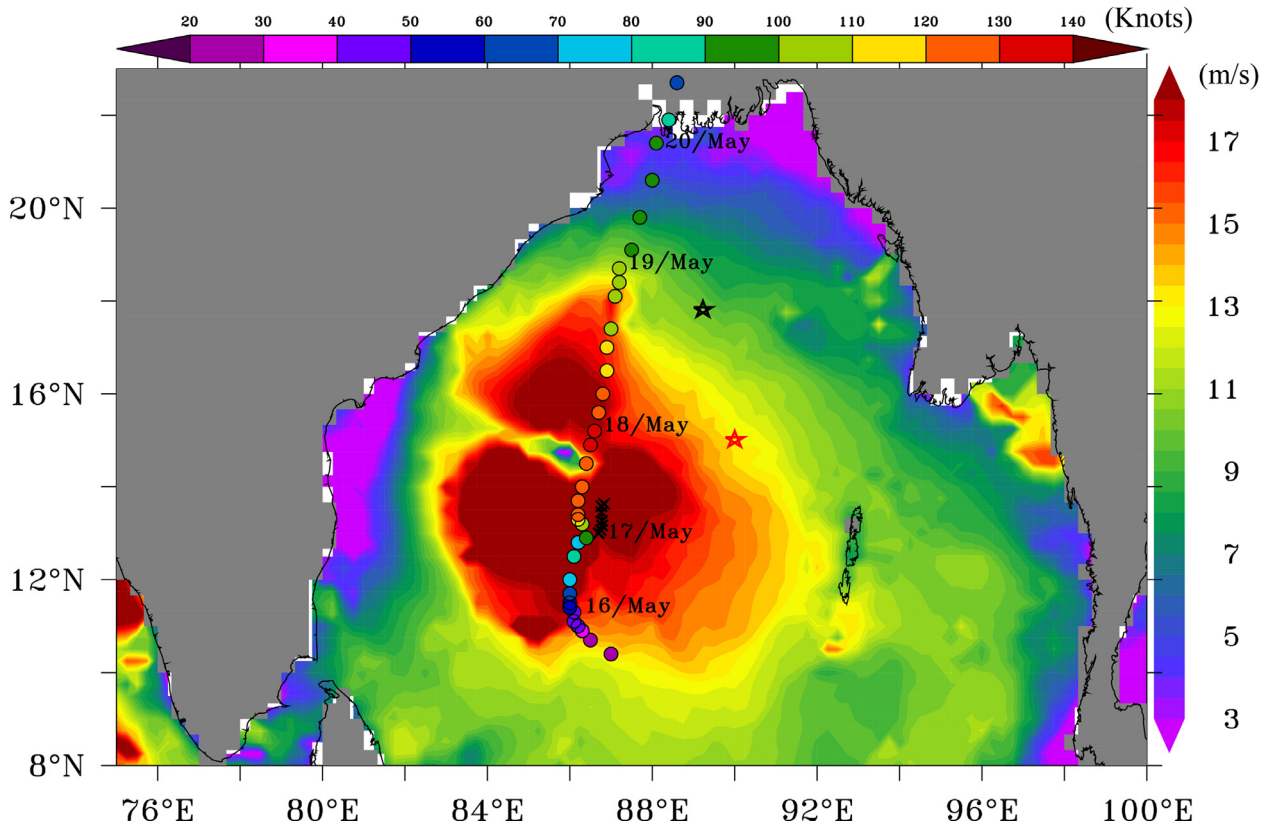

Figure 1 The study area and the track of cyclone Amphan overlaid over the wind distribution (m/s) on 18 May 2020 on which cyclone Amphan experienced the peak intensity. The location of the cyclone on each day at 21:00 UTC is indicated by the corresponding dates. The colours on the cyclone track indicate the maximum surface wind speed of the cyclone (knots). The black and red stars denote the locations of the moored buoy BD8 and Rama mooring respectively. The black cross signs denote the position of the Argo float (2902230) during May 2020.

(Kara et al., 2000). The Ekman pumping velocity (WE) is calculated as

$$WE = \frac{1}{\rho f} Curl(\tau) \tag{1}$$

where ρ is the density of the sea water set to 1025 kg /m^3, τ is the wind stress, f is the Coriolis parameter. The vertically integrated ocean heat content (OHC) is computed with the equation,

$$\mathrm{OHC} = \rho C_p \int T dz \tag{2}$$

where ρ and C_p are the density and heat capacity of sea water for which the values used in this study are 1025 kg/m^3 and 4000 J/kg/K respectively and z is the water depth. In order to examine the response to Amphan, 7 days before the Amphan (9–15 May) was considered as the pre-cyclone period and 7 days after Amphan (21–27 May) was considered as the post-cyclone period. The difference between these two periods was chosen to evaluate the response of the parameters considered.

To examine the relative roles of the various processes that contributed to the changes in mixed layer temperature and salinity, mixed layer heat and salinity budgets were evaluated following Rao and Sivakumar (2000) and Chacko et al. (2012) using the following set of equations:

$$\frac{\partial T}{\partial t} = \frac{Q_{net} - Q_{pen}}{h\rho C_p} - \left[u\frac{\partial T}{\partial x} + v\frac{\partial T}{\partial x}\right] - H\left[w_h + \frac{dh}{dt}\right] \times \frac{(T - T_h)}{h} \tag{3}$$

The terms in the equations represent from left to right, the mixed layer temperature tendency, surface net heat flux term, horizontal advection term and vertical processes term.

$$\frac{\partial S}{\partial t} = \frac{(E - P)S}{h} - \left[u\frac{\partial S}{\partial x} + v\frac{\partial S}{\partial x}\right] - H\left[w_h + \frac{dh}{dt}\right] \times \frac{(S - S_h)}{h} \tag{4}$$

The terms in the mixed layer salinity budget equation represent from left to right, the mixed layer salinity tendency, Evaporation minus Precipitation (E-P) term, the horizontal advection term, and the vertical processes term. The vertical processes are due to a combination of entrainment at the base of the mixed layer and upwelling. In Eqs. (3) and (4), ρ is the density of seawater, C_p is the specific capacity of sea water (4000 J/K/kg); T and T_h are mixed layer temperature and temperature at a depth 5 m below the mixed layer (h); S and S_h are mixed layer salinity and salinity at a depth 5 m below the mixed layer (h); u and v are the

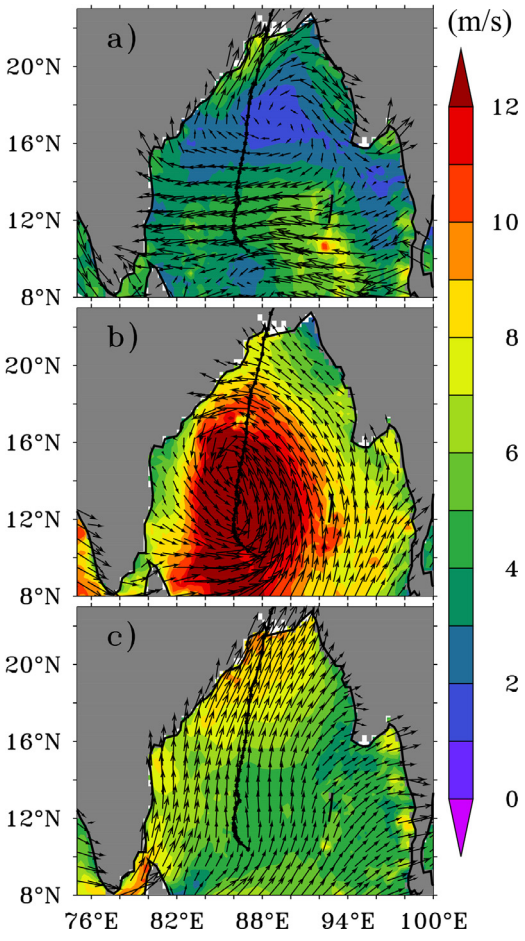

Figure 2 Daily sea surface wind speeds from Scatsat-1 a) before (10–15, May 2020), b) during (16–20, May 2020) and c) the difference for (b) minus (a) of cyclone Amphan. The colour contours show the wind speeds, and the arrows show the direction of the winds at that location.

zonal and meridional currents; w_h is the vertical velocity at the thermocline below the mixed layer; $\frac{dh}{dt}$ is the variability of the mixed layer depth. Here H is a scale factor which is taken as 1 if $[w_h + \frac{dh}{dt}]$ is positive and 0 if $[w_h + \frac{dh}{dt}]$ is negative. The net heat flux at the surface (Q_{net}) is given by $Q_{swf}-Q_{lwf}-Q_{sen}-Q_{lat}$, where, Q_{swf} is shortwave flux, Q_{lwf} is longwave radiation, Q_{sen} is sensible heat flux, and Q_{lat} is latent heat flux. Penetrative solar radiation Q_{pen} is the solar radiation at the base of the mixed layer and it is estimated as $Q_{pen}=Q_{swf}(1-R)\ e(-h/\zeta)$, where R =0.58, the radiation lost by getting absorbed in the upper layers (Paulson and Simpson, 1977), h the mixed layer depth, and ζ the attenuation depth. For computing horizontal advection, sea surface temperature and sea surface salinity gradients are calculated using AMSR-2 sea surface temperature and SMAP sea surface salinity as centered differences over a distance of 0.25° from the moored buoy BD8 location.

3. Results

3.1. Tropical cyclone Amphan

Tropical cyclone Amphan originated from a low-pressure region over east of Sri Lanka in the southeast BoB on 16 May 2020. It moved north-eastward and intensified into a cyclonic storm on 16 May. Afterwards, it moved northwards and further intensified into a severe cyclonic storm on 17 May. It underwent rapid intensification within a few hours and became a super cyclone on 18 May. It maintained the intensity of the super cyclone over west central BoB before weakening into an extremely severe cyclonic storm on 19 May. Amphan made landfall across the Sunderbans and crossed West-Bengal and Bangladesh coasts on 20 May with maximum sustained wind speeds of 155–165 kmph. Figure 1 shows the study area as well as track of the super cyclone along with wind speeds over the BoB. The locations of the Argo float, moored buoy (BD8) and the RAMA buoy during cyclone Amphan are also shown in the figure.

The surface wind fields that were prevalent before and during Amphan are shown in Figure 2. The background wind speeds before the cyclone (Figure 2a) were predominantly easterly in the central BoB. In the northern BoB (north of 15°N latitudes), the wind speeds were slightly weaker (1–4 m/s) than in the southern BoB. Figure 2b shows the wind speeds during cyclone Amphan wherein, the wind speeds were significantly higher, reaching >12 m/s all along the west-central BoB. The magnitude of wind speed was stronger on the right side of the track of the cyclone. The anticlockwise circulation of the cyclonic wind fields was clearly visible in the figure. Post-cyclone, the wind fields were observed to be reduced to < 8 m/s in the entire BoB and the direction of the wind vectors were aligned south westerly in accordance with the prevailing monsoonal wind systems during that period.

3.2. Upper ocean response to Amphan

The temporal evolution of major atmospheric and oceanic surface variables obtained from the RAMA buoy are shown in Figure 3. The sea level pressure before the cyclone was around 1009 hPa accompanied by moderate winds of 2 to 4 m/s (Figure 3a,b). Before the cyclone, there was no rainfall event (Figure 3e) and the air temperature was in the range 30 to 30.5°C (Figure 3c). The sea surface temperature was greater than 31°C and the sea surface salinity was ~33 PSU (Figure 3d,f). The effect of the super cyclone could be clearly inferred from the observations of the buoy during 16–20 May. During the passage of Amphan, the sea level pressure rapidly dropped to 994 hPa on 18 May. The surface winds before Amphan were ~4 m/s which is consistent with the satellite observations in (Figure 2) that increased significantly to 15 m/s (Figure 3b). In response to the cyclone, the air temperature dropped from 30°C to a minimum of 27°C, sea surface temperature decreased from the pre-cyclone value of 31.5°C to 29°C, and the sea surface salinity increased from 33.17 PSU (15 May) to 33.34 PSU (21 May). The sea surface cooling was essentially very high ~2°C compared to the pre-Amphan values.

3.3. Sea Surface Temperature

To explore the spatial and temporal features of the surface ocean response to Amphan, multiple satellite observations were employed. First, we assessed the response of sea surface temperature using satellite observations. Figure 4 il-

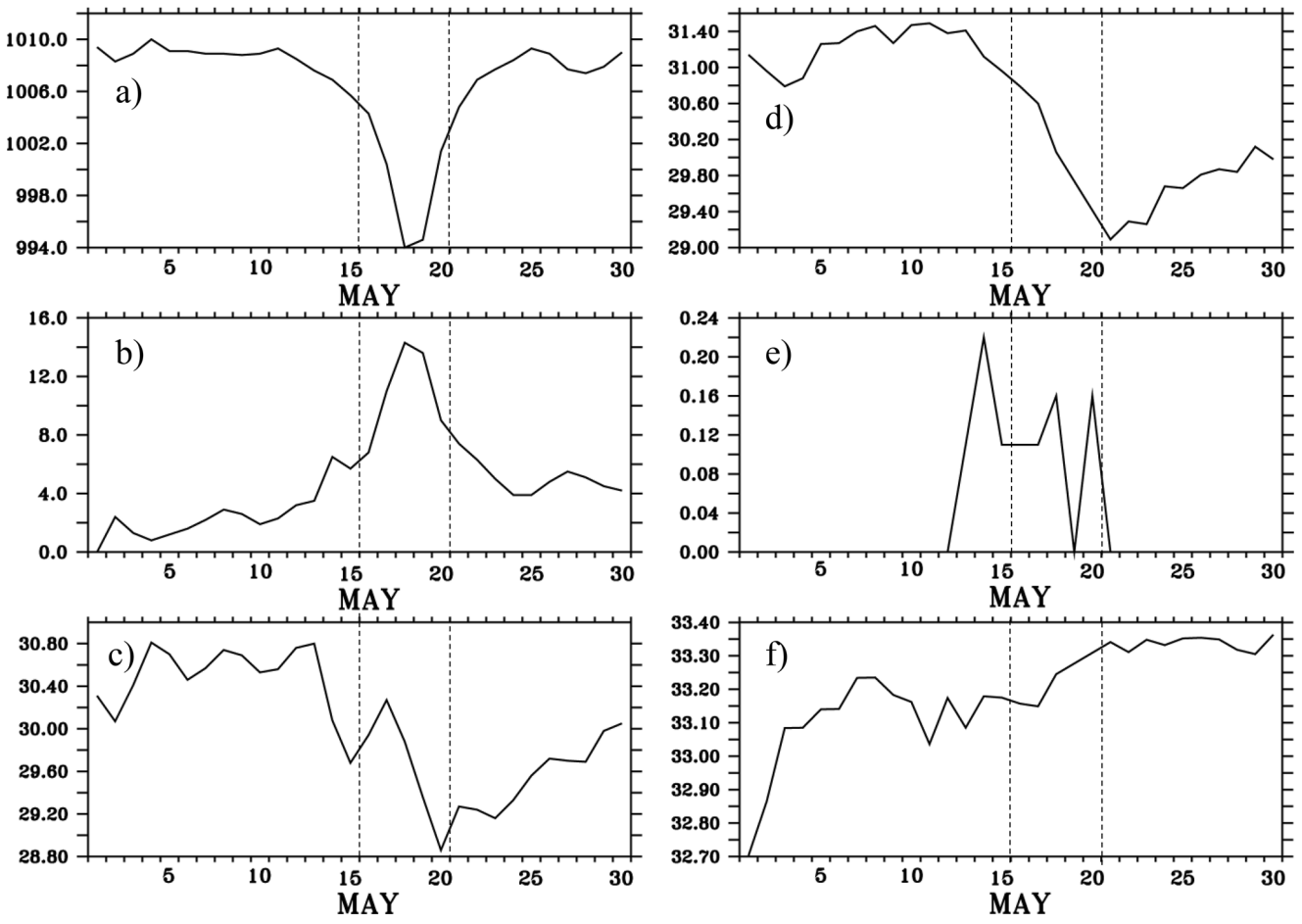

Figure 3 Meteorological and oceanographic parameters observed from a RAMA buoy located at 90°E longitude, 12°N latitude from 01—31 May 2020. a) Sea level pressure (hPa), b) surface wind speed (m), c) air temperature (°C), d) Sea surface temperature (°C), e) rainfall (mm/hr) and f) sea surface salinity (PSU). The period of activity of Amphan was 16—20 May 2020 which is indicated by vertical lines on each plot.

lustrates the sea surface temperature response due to Amphan in the BoB that was evident from AMSR-2 data. Before the arrival of Amphan, the entire BoB was capped by warm surface waters, with sea surface temperatures greater than 31°C (Figure 4a). It was observed that Amphan originated in the southern BoB, over warmer waters. The passage of Amphan cooled the ocean surface substantially (Figure 4b) compared to the pre-Amphan sea surface temperature with distinct magnitudes across the basin. The difference between the post-cyclone and pre-cyclone sea surface temperature clearly depicted the extent of the cold wake left by Amphan (Figure 4c). There were many studies which reported on the strong sea surface cooling by cyclones (Navaneeth et al., 2019; Qiu et al., 2019), but a cold wake extending over the entire BoB is a rarity. A strong sea surface temperature cooling spread over a large area with a slight rightward bias to the track of Amphan could be seen in Figure 4c. The rightward bias shown in the sea surface temperature cooling was consistent with the previous studies (Black and Dickey, 2008; Chu et al., 2000; Yue et al., 2018). It was mainly due to the fact that the cyclone induced wind stress vector turns clockwise on the right side of the cyclone track and resonate with the mixed layer current (Cheung, et al., 2013; Price, 1981). Though cooling was spread over the entire BoB, strong decrease in the sea surface temperature (∼4°C) was observed along the central BoB, where the cyclone exhibited its strongest wind speeds during its lifetime (see Figure 1).

3.4. Sea Surface Salinity

The sea surface salinity maps before and after Amphan are shown in Figure 5a and b. Before cyclone (Figure 5a), there was an east-west salinity gradient in the BoB with higher salinity (>33.5 PSU) in the western Bay and lower salinity (Value) in the eastern BoB. The northern BoB showed very low salinity values (< 30 psu) owing to the high freshwater influx into the region from the rivers. After Amphan, the sea surface salinity was observed to have increased (1 PSU) (Figure 5b). Figure 5c illustrates the Amphan induced salinity changes and it could be observed that sea surface salinity in the regions right of the track of the cyclone had increased compared to the left side of the track. The maximum salinity increase was ∼1.5 PSU to the right side of the Amphan track along the central Bay. This is consistent with the observation of Chacko (2018) which reported that

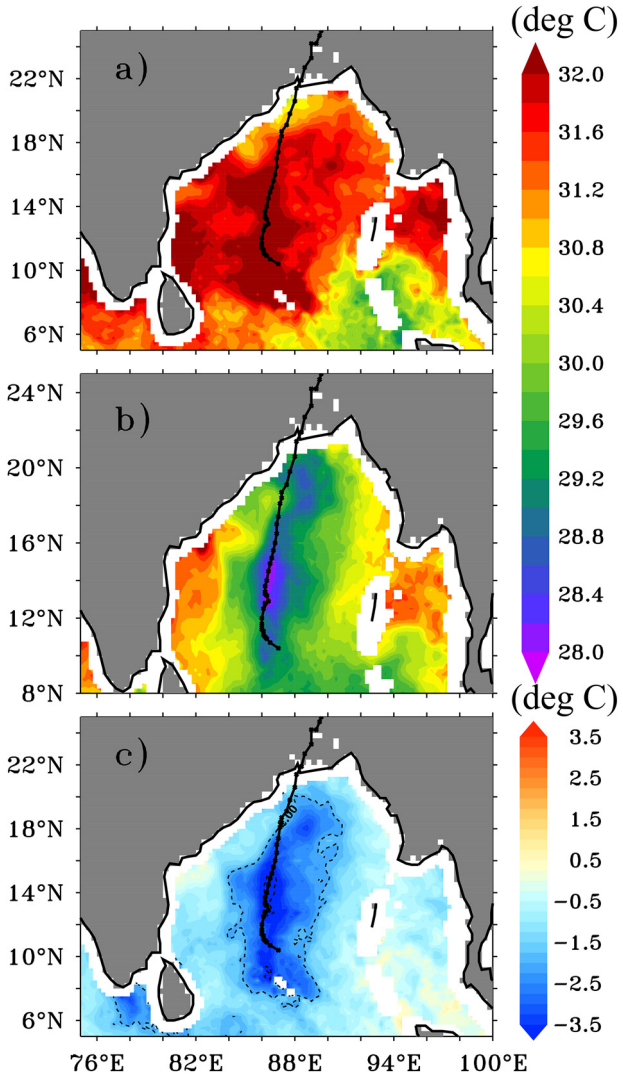

Figure 4 AMSR-2 sea surface temperature (°C) averaged for the periods: a) Pre-Amphan (10—15 May), b) post-Amphan (21—28 May), c) the difference for (b) minus (a). The track of Amphan is overlaid on each plot. The dashed lines overlaying on (c) indicate 2°C isothermal contours.

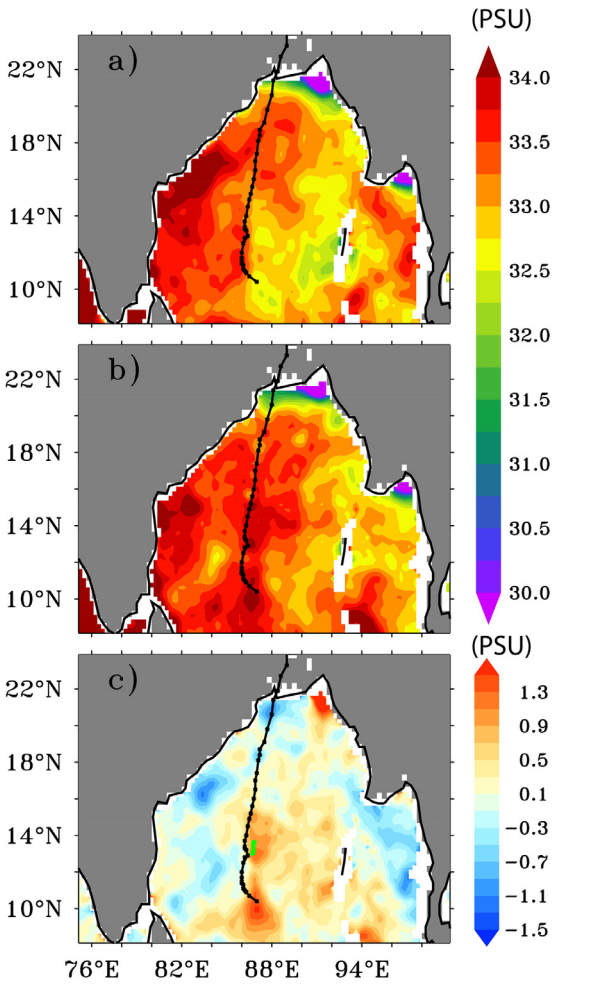

Figure 5 SMAP level-3 8-day running mean sea surface salinity (PSU) showing the a) pre-cyclone b) postcyclone and c) post-cyclone minus pre-cyclone salinity. The location of the Argo float is overlaid on (c) as green dots (Qiu et al., 2019).

cyclone Vardah (2016) induced a significant increase of surface salinity on the right side of the storm using SMAP salinity data. In contrast, only a weak drop in salinity (~0.7 PSU) was found over most regions to the left of the track of Amphan. The rainfall rate measured by AMSR-2 (Figure 6) indicates high rainfall along the left of the track of Amphan (3—6 mm/hr) than the right side of the track. Previous studies had reported on this asymmetric rainfall distribution during cyclones is due to the vertical wind shear, topography and water vapor flux (Burpee and Black, 1989; Chacko, 2018; Chen et al., 2010; Corbosiero and Molinari, 2003; Yue et al., 2018). The influx of fresh water from the intense precipitation was responsible for freshening on the left side of the track.

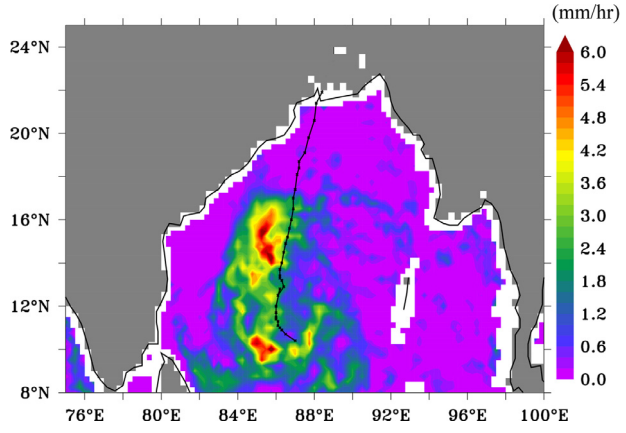

Figure 6 AMSR-2 measured rainfall rate during the period of Amphan (16—20 May 2020).

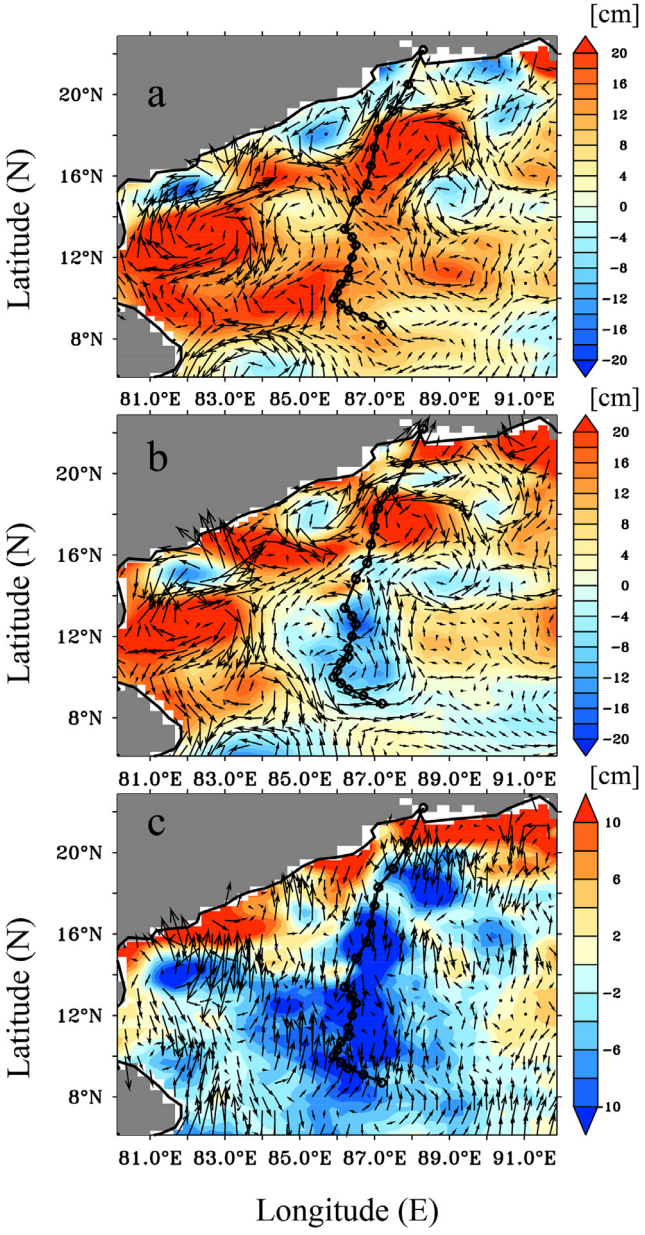

Figure 7 OSCAR surface currents (cm/s) overlaid on mean sea level anomalies (coloured fields, cm) during a) pre-Amphan, b) post-Amphan, and c) pre-Amphan minus post-Amphan.

3.5. Sea Surface Currents

Upper ocean current response to Amphan is characterized using OSCAR currents. Figure 7 shows the surface current speeds overlaid on the mean sea level anomaly during the periods before and after the cyclone. It could be seen that the pre-Amphan periods were characterised by strong positive sea level anomalies that depicted warm core regions. This also implied the presence of warmer subsurface waters before the cyclone. The sea surface currents were distributed along the warm core regions with speeds greater than 50 cm/s. The strong surface winds of the cyclone could modulate the near surface ocean currents. Figure 7b shows the surface currents during the post-Amphan period. Note that the increase (decrease) of the surface winds always depends on the direction of the wind vector. If the current and wind vectors are in the same direction, the current increases and vice versa. This is illustrated in Figures 7a and b, wherein the southward strong surface currents that prevailed during the pre-Amphan period in the central BoB were observed to be reduced in their magnitude. This was because the surface currents were in the opposite direction (southwards) to that of the cyclonic winds (northwards). The surface currents in the southern BoB however, have increased in magnitude compared to the pre-Amphan conditions. The maximum enhancement of the surface currents due to Amphan happened on the right side of its track. This was because, in the right-hand side of the cyclone track, the inertial forces turn the ocean currents in the same (opposite) direction as the wind stress in the right (left) side of the track (Zhang et al., 2020). This illustrates that the surface currents also exhibited rightward bias under the cyclonic forcing, similar to the other analysed parameters.

The variability of subsurface currents due to Amphan was also studied using the moored buoy (BD8) data (location of the buoy is provided in Figure 1). During the passage of Amphan, the current speed at all depths was observed to rise in response to the increase in wind speed (Figure 8a,b). Amphan increased the subsurface current speed to ∼130 cm/s from the pre-cyclone values of ∼25 cm/s. The surface and subsurface currents are observed to be restored to the pre-cyclone values by 26 May, 6 days after the cyclone passed over the buoy. The pattern of variability of the surface and subsurface currents induced by Amphan is similar. The maximum current speed of 130 cm/s was recorded at the buoy location on 20 May. A lag of 2 days can be noted between the maximum increase in wind and current speeds as evident from the observations. Figure 8c shows the direction of surface current measured by the buoy. South-southwestward current with an average speed of 20 cm/s is observed at the buoy location before Amphan (Figure 8b and c). The current direction plotted in Figure 8c shows the clockwise rotation of the currents during the period 19—26 May. The existence of near inertial oscillations is reported after the passage of cyclones (Joseph et al., 2007). The near inertial period at the buoy location is 15.9 hours given by $2\pi/f$ where f is the Coriolis parameter. The periodicity of the surface currents computed using Fast Fourier Transform method given in Figure 8d shows 13 hours closely matching with the theoretical values. In the northern hemisphere, the inertial oscillations are clockwise. The inertial oscillations that are forced by Amphan disappeared on 26 May, lasting for ∼9 inertial periods after its passage.

3.6. Chlorophyll concentration

Satellite derived ocean colour chlorophyll will have limited coverage due to cloud cover. During cyclone time, the coverage will be much hampered. To assess the biological changes induced by Amphan, surface chlorophyll concentration from VIIRS was used (Figure 9). From the 8-day chlorophyll-*a* data, it could be seen that during the pre-cyclone period, the chlorophyll values were in the range of 0—0.2 mg m^{-3} (Figure 9a), very less values which was typical of the oligotrophic BoB. Post-cyclone, while the data

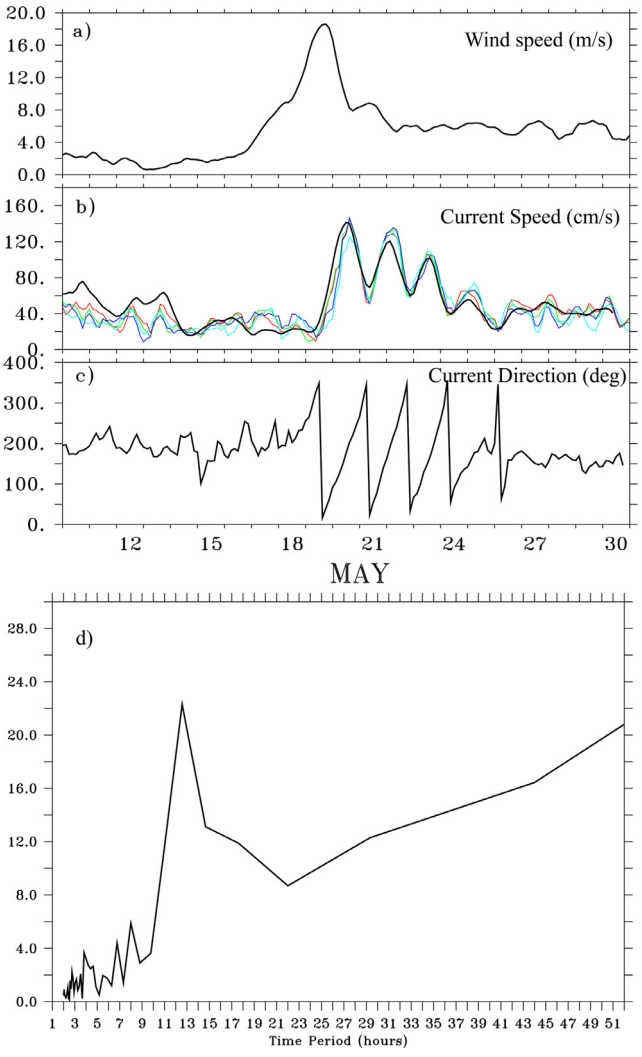

Figure 8 Observed time series of a) wind speed (m/s); b) current speed at different depths (cm/s) at the surface (black), 15 m (red), 25 m (green), 35 m (cyan); c) current direction (degrees) at the surface measured by moored buoy BD8; d) Fast Fourier Transform of the surface current during Amphan observed from the moored buoy BD8.

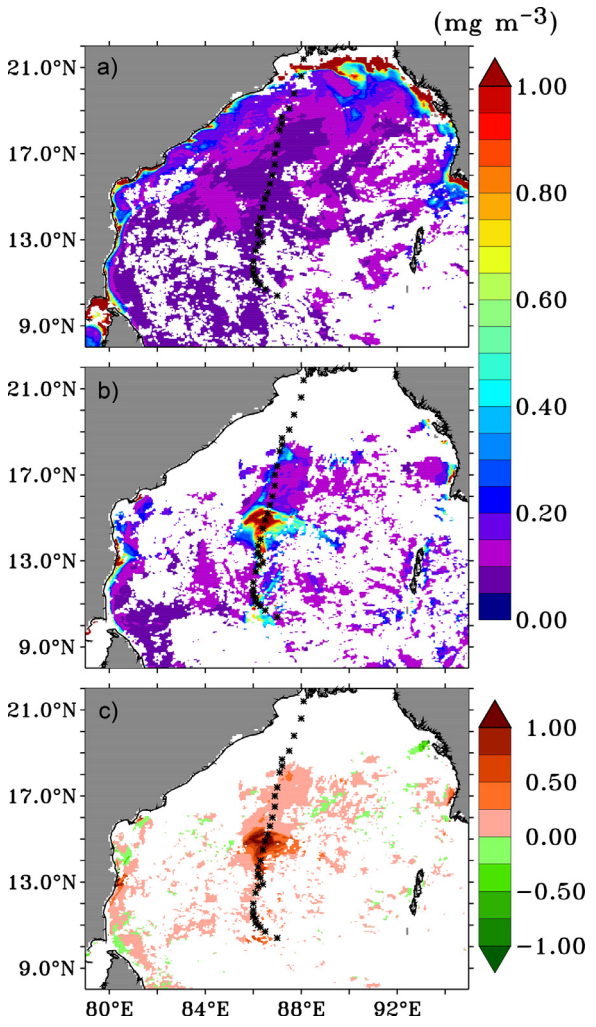

Figure 9 VIIRS chlorophyll concentration (mg/m^3) averaged over a) pre-Amphan (7—15 May), b) post-Amphan (24—31 May) and c) the difference post-Amphan minus pre-Amphan.

coverage over most of the regions over the BoB were hampered by cloud cover, in the central Bay, the signatures of a strong bloom could be observed. Chlorophyll concentration increased markedly after the passage of the cyclone from an average value of ∼0.1 mg/m^3 to ∼1.5 mg/m^3 (Figure 9b,c). A visual comparison of Figure 4c and Figure 8c shows that regions of higher chlorophyll were collocated with that of regions where cooling was maximum. The region of chlorophyll enhancement was also collocated with the region where the cyclone exhibited its highest maximum sustainable wind speed of 245 km/h (18 May). Thus, tight coupling exists between changes in sea surface temperature, chlorophyll and the wind forcing. This substantiates the impact of wind induced vertical mixing and upwelling in elevating higher chlorophyll concentration and reducing sea surface temperature. This also shows that the positive surface chlorophyll concentration observed after passage of Amphan was dominated by vertical processes such as entrainment and upwelling.

3.7. Subsurface response

In order to examine the subsurface temperature and salinity response to Amphan, observations from an Argo float and a moored buoy were employed. The Argo float was located very near to the track, within 50 km from the eye of the cyclone and the moored buoy was located ∼3 degrees away from the track. So, this provided a unique opportunity to assess the difference in oceanic response induced by Amphan at different locations away from the track. The temporal evolution of temperature and salinity profiles from Argo float are shown in Figures 10a and b. The mixed layer depth before Amphan was relatively shallow, in the range of ∼15 m depth. Below the mixed layer, relatively colder and saltier waters prevailed before the passage of Amphan (Figures 10a and b). A decrease in the temperature in the upper 100 metre depth is shown in Figure 10a after 16 May which was attributed to the cyclone forcing. The depth of the mixed

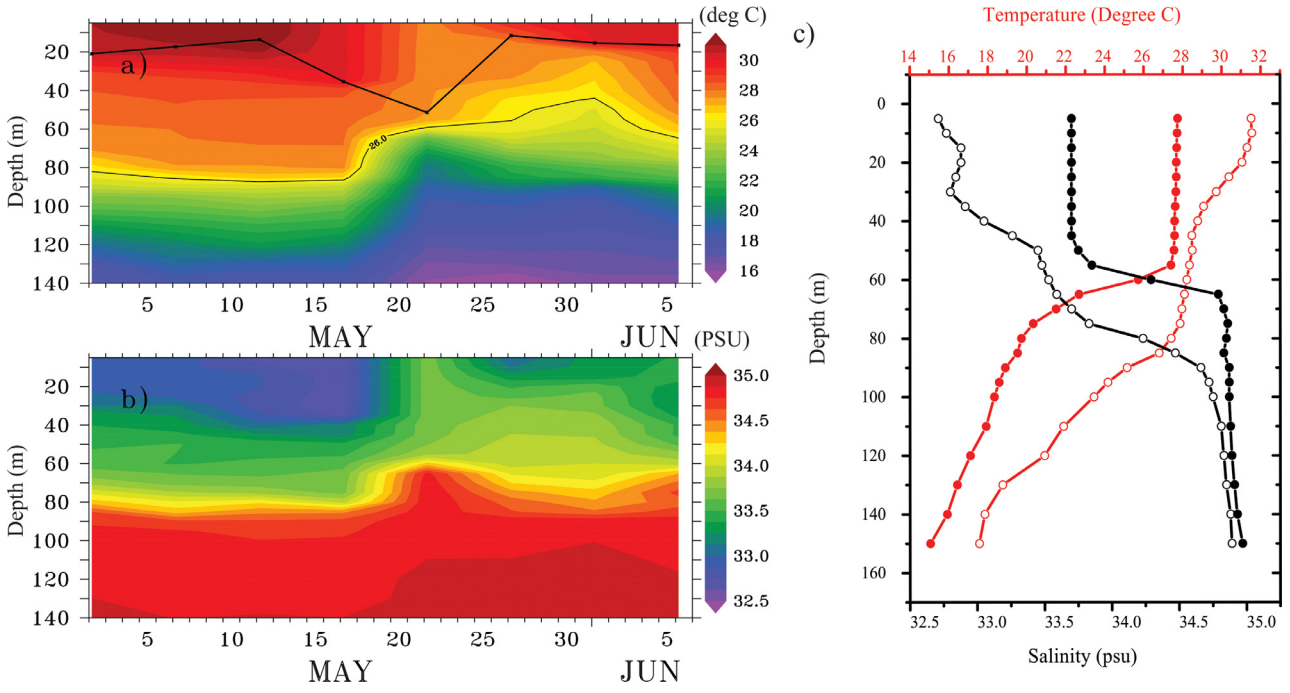

Figure 10 Subsurface a) temperature (°C) and b) salinity (PSU) from Argo float (WMO id 2902230). The thick and thin black lines in a) are mixed layer depth (m) and depth of 26°C (m) isotherm respectively. c) Temperature (red) and salinity profiles (black) observed by Argo float. Open and closed circles represent pre-cyclone and post-cyclone periods respectively.

layer was observed to have increased from 20 m to 55 m by 20 May. Deepening of the mixed layer is the manifestation of the entrainment and mixing that is induced by the current shear due to the cyclone forcing. Depth of the 23°C isotherm is considered as a proxy for the thermocline depth, and had shoaled from 80 m (pre-Amphan) to 60 m (post-Amphan) (Figure 10a). This deepening of the mixed layer and the rising of thermocline was due to strong vertical mixing induced by the super cyclone. The upper ocean temperature decreases with the cyclone forcing as the mixed layer deepened. While it could be seen that after the cyclone passage, the surface temperatures started to warm more rapidly than subsurface waters, eventually the sub-surface water column also appeared to restore to their pre-cyclone values within 2 weeks after the passage of Amphan. The impact of Amphan was clearly visible throughout the upper 150 m depth of the ocean in the Argo observations.

Unlike the reduction in the ocean temperature, ocean salinity was observed to increase after the passage of Amphan (Figure 10b). The Argo float was located on the right side of the track of Amphan and the observed response of salinity was consistent with the increase in surface salinity observed from the satellite data. The vertical mixing causes the saline sub-surface water to advocate to the surface, causing the upper ocean salinity to increase from the pre-cyclone values of 33 PSU to 34 PSU that are consistent with the satellite observations of surface salinity change. After the cyclone, the near surface salinity was observed to have reduced to 33.5 PSU. This could be due to the advection of fresh surface water resulted from the cyclone induced precipitation. The increase in surface salinity lasted for a week and was restored to pre-cyclone values by 27 May. However, the subsurface salinity was not restored until the first week of June. Recovery time of salinity is reported to take weeks after the passage of cyclone (Du and Park, 2019; Sun et al., 2021). The variations of temperature and salinity profiles before and after the cyclone observed from the Argo float are shown in Figure 10c. The pre-cyclone salinity profile showed the salt-stratified barrier layer in the near surface below the thin mixed layer. The vertical mixing induced by Amphan brought the higher saline waters from the barrier layer to the surface that resulted in intense post-cyclone surface salinity enhancement. The mixed layer increased to 50 m depth after the cyclone (Figure 10c). Figure 5c depicts saltier waters along the location of the Argo float. This significant salinity increase at this region could be attributed to the intrusion of saltier water present just below the surface layer. Increase in the magnitude of salt wake in the regions with higher vertical salinity gradient below the mixed layer was reported by Reul et al., (2021) and Sun et al., (2021).

The temperature and salinity observed by the moored buoy BD8 is shown in Figure 11a. The buoy was farther to the cyclone track, yet the influence of the cyclone was evident in the temperature and salinity fields. The warmer near surface water layer was cooled under the influence of Amphan. The initial mixed layer depth before Amphan was shallower over this region (15 m), which deepened to a depth of 60 m under the cyclone forcing. The deepened mixed layer depth suggested strong vertical mixing induced by Amphan. Prior to Amphan, salinity in the near surface layer was low (32.9 PSU). The salinity rapidly increased to 33.6 PSU by 18 May which suggested that subsurface salty waters were mixed or uplifted to the surface (Figure 11b). Increase in salinity and decrease in temperature was observed at the buoy location, concurrent to the observations from Argo.

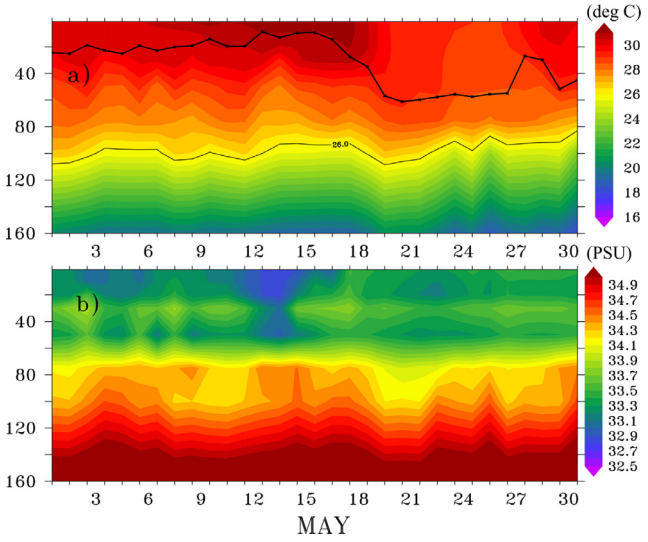

Figure 11 Observations of a) temperature (°C) and b) salinity (PSU) from moored buoy BD8. The thick and thin overlaying lines on a) represent mixed layer depth and the depth of 26°C isotherm respectively.

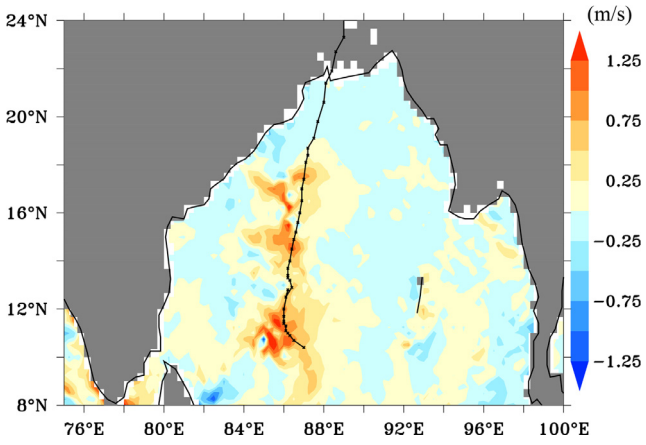

Figure 12 Ekman pumping velocity (m/s) during Amphan (16—20, May 2020) computed from SCATSAT winds.

However, the thermocline depth variability depicted by the depth of the 26°C isotherm showed slight deepening during the cyclone period, contrasting the observations from Argo wherein, the thermocline shoaled during the cyclone (Figure 10a). The thermocline displacement is a manifestation of the upwelling process which brings subsurface waters to the surface under strong wind forcing. The thermocline displacements due to Amphan at the location of Argo was computed from the wind stress using the relation $\eta = \tau/(\rho f T_s)$ (Price, 1981), where η is the thermocline displacement, τ is the wind stress, ρ is the sea water density, f is the Coriolis parameter, and T_s is the translation speed of the cyclone. The thermocline displacement estimated at the Argo location was 14 m. This was consistent with the observed thermocline displacement of ∼16 m (Figure 10a).

The rising (deepening) contours of the thermocline depicts upwelling (downwelling) induced by the cyclone. The strength of the upwelling can be understood from the Ekman pumping velocity, the positive (negative) Ekman pumping velocity indicates upwelling (downwelling). Figure 12 shows the Ekman pumping velocity during the Amphan cyclone which was computed from Scatsat-1 wind data. Positive Ekman pumping velocity along the track of Amphan inferred the upwelling induced by the cyclone. Considerable difference in the Ekman pumping velocity was seen at the locations of Argo and BD8. At the location of Argo float, strong Ekman pumping velocity and at the location of moored buoy negative Ekman pumping velocity prevailed during Amphan. This corroborated the fact that at the location of BD8, Amphan did not induce upwelling. Thus, it appears that at the location of Argo both entrainment and upwelling processes contributed to the observed near surface cooling and increase in salinity. Also, it is evident from Figure 1 and Figure 2 that the wind speeds at the locations of Argo float and BD8 were different. Argo float was located where the cyclone had its maximum wind speeds and BD8 was located at the region where the cyclone had relatively lower wind speeds. It is also worth to note that the translation speed of Amphan was significantly different in its later course than during its initial course. Figure 1 clearly depicts the same. Above (below) 16°N latitudes, Amphan traveled faster (slowly). The translation speed of Amphan was higher at the location of the moored buoy, and slower at the Argo. It is reported that upwelling has negligible role in reducing the sea surface temperature for fast moving cyclones, whereas for slow moving cyclones it plays important role (Behera et al., 1998; Bender et al., 1993; Black, 1983; Lin, 2012; Price, 1981). The strong winds and slower translation speeds could be presumed as the reason for inducing strong vertical entrainment and upwelling at the Argo location and similarly, weaker winds and faster translation speeds the reason for failing to induce upwelling at the moored buoy location.

Strong winds induced by the super cyclone pumped cold and salty, deeper waters to the near surface layers, which resulted in the cooling of sea surface temperature and increased surface salinity at the Argo location. The subsurface cooling was also evident in the OHC computed from the Argo measured subsurface temperature. The depth of the vertical mixing induced by Amphan was approximated as 150 m based on Figure 9 and the OHC was computed over 150 m depth of the water column. The Argo measured OHC decreased from 1.6×10^{10} J/m^2 to 1.4×10^{10} J/m^2 (Figure 13). This shows that the subsurface lost heat during the cyclone. As heat from the ocean provides energy to cyclones, it is expected to have loss of ocean heat content after the cyclone.

4. Discussion

To explore the causes for the variations in the mixed layer temperature and salinity during the cyclone forcing, heat and salinity budget estimations are conducted using the observations at BD8 owing to its high temporal resolution compared to Argo. The impact and relative roles of the major processes on the mixed layer temperature and salinity changes can be deciphered from the budget estimations. Post-cyclone sea surface temperature cooling is a very complex process, involving hydrodynamic (entrainment and up-

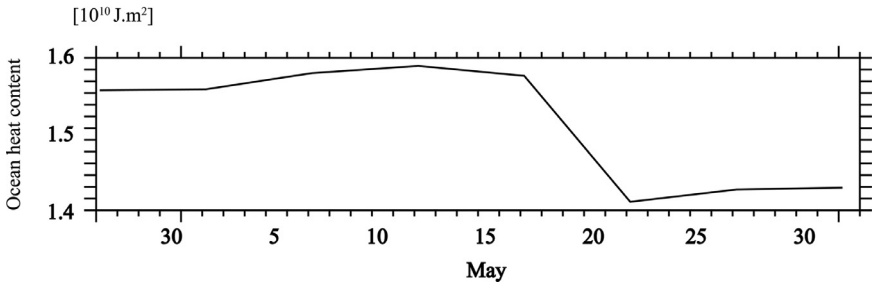

Figure 13 Ocean heat content (J/m^2) up to 150 m depth of the vertical water column estimated from Argo temperature fields.

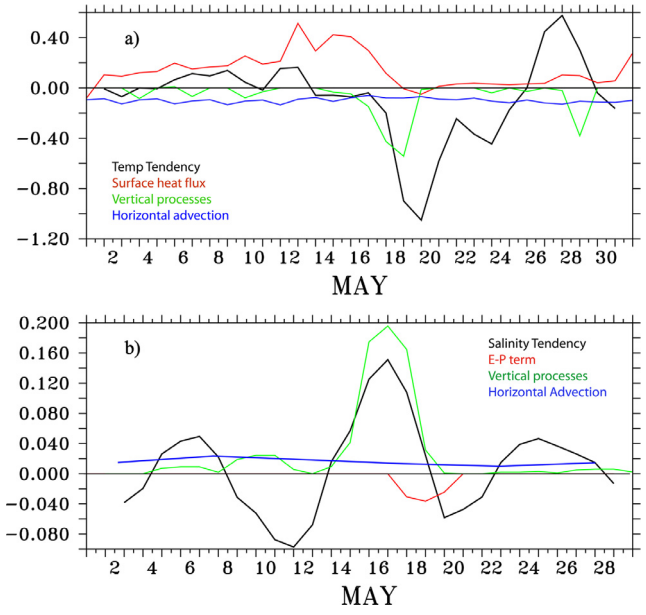

Figure 14 a) Mixed layer heat budget and b) mixed salinity budget terms computed from observations from moored buoy BD8.

welling) and thermodynamic processes (surface heat flux). The time series of each term from the heat budget estimation is presented in Figure 14a. The various terms of the heat budget equations: temperature tendency, net heat flux term, vertical processes and horizontal advection are plotted in the figure. Before the passage of Amphan, slight warming (∼0.18°C/day) was observed in the mixed layer temperature consistent with the pre-cyclone warmer surface waters as presented in Figure 14a. With the advent of Amphan, the mixed layer temperature tendency showed strong cooling (−1.1°C/day) from 16—20 May. The cooling continued varying in magnitude in the following days and by 26 May the mixed layer temperature tendency appears to reverse the sign, implying recovering to the pre-storm conditions. The surface net heat flux term is observed as having strong influence in warming the mixed layer temperature before the period of Amphan. However, a considerable reduction in the surface net heat flux occurred during the cyclone and it remained low until 26 May. The contribution of horizontal advection term on the heat budget was observed to be having far smaller contributions (−0.1°C/day) but indicative of cooling the mixed layer temperature. In contrast, a far stronger cooling was seen from the vertical processes (−0.6°C/day) during Amphan. Entrainment and upwelling contributed to the vertical processes term in the heat budget equation. The combined effect of these two processes induced mixed layer temperature tendency in general. As shown in the Section 3.7, at the location of BD8, the depth of the 26°C did not shoal and the Ekman pumping velocity was weakly negative. This indicates that Amphan did not induce upwelling at this location and hence the contribution of entrainment cooling was much stronger at this location. The observed strong mixed layer cooling ceases by 26 May. Therefore, the mixed layer heat budget estimations showed that the strong cooling induced by Amphan at this region was due to the combined contributions of vertical processes and horizontal advection. As shown in Section 3.7, at the location of the moored buoy, cyclone could not induce upwelling. The major contributor of the cooling can be attributed to the vertical entrainment from below the mixed layer.

A mixed layer salinity budget estimation was carried out to examine the roles of processes, which determine the salinity variability. The processes considered are Evaporation minus Precipitation ($E - P$), vertical processes, and horizontal advection. These terms along with mixed layer salinity tendency are illustrated in Figure 14 b. The mixed layer salinity tendency oscillates between increase and decrease during the month of May. The amplitude of oscillation is significantly positive during Amphan (16—20 May) reaching 0.160 PSU/d. The $E - P$ term showed negative tendency during Amphan attempting to reduce the mixed layer salinity. The precipitation induced by the cyclone tries to freshen the salinity. Horizontal advection term is slightly positive trying to increase salinity through the month of May. The term due to vertical processes appears to have a significant contribution during the cyclone period (0.19 PSU/d). The significant increase in salinity during Amphan was observed due to the vertical processes. While $E - P$ term tries to freshen the mixed layer salinity, combined contribution from vertical processes and horizontal advection results in a net increase in the mixed layer salinity. The two mixed layer budget analysis at the location of BD8 indicates that the vertical entrainment was the major contributor in inducing an increase in salinity and decrease in temperature.

Very few studies examined the mixed layer heat and salinity budget equations during cyclones in the Indian Ocean. Girishkumar et al. (2014) observed that vertical mixing was the dominant factor which controlled the sea surface cooling in the case of cyclone Jal which occurred in the year 2010. Prakash and Pant (2017) showed using numerical modelling that the sea surface temperature cooling

during cyclone Phailin was due to the combined effect of horizontal advection and vertical mixing with stronger contribution from horizontal advection. Our results showed that vertical processes are the significant contributor in decreasing the mixed layer temperature and increasing the mixed layer salinity. This result is contradicting the previous study by Prakash and Pant (2017), and agrees well with the study of Girishkumar et al. (2014).

The post-Amphan surface chlorophyll bloom is observed along the regions where the Amphan had highest wind speeds. This anomaly (Figure 9c) of higher chlorophyll concentration is consistent with the studies of Chacko (2017); Gierach and Subrahmanyam (2008) and Walker et al. (2005) which reported on surface chlorophyll blooms near the trajectory of the cyclones. The areas of strong cooling and higher chlorophyll concentration are spatially collocated, which can be seen in the spatial plots in Figure 4 and Figure 9c. This is due to the fact that the physical mechanism which results in the variability of these two parameters are the same. i.e., vertical mixing due to the strong cyclone winds. The vertical mixing induced by the cyclone winds brings cooler subsurface waters which are also rich in nutrients and chlorophyll content into the surface waters. Thus, the sea surface cooled and the chlorophyll concentration increased after Amphan. However, the surface salinity variability after the cyclone was different compared to the sea surface temperature and chlorophyll concertation. This is because in addition to the vertical processes, strong rainfall induced by the cyclone also played a key role in the salinity variability. The net result in the salinity will be the resultant between these two opposing processes. Hence the areas of cooling and increase in salinity does not match unlike areas of cooling and chlorophyll bloom.

Satellite observations revealed that the wake of the super-cyclone Amphan was apparent in the sea surface temperature, sea surface salinity, chlorophyll concentration, and on the surface currents. It is also evident from the spatial picture of the parameters assessed that the pronounced variability was observed in the central Bay of Bengal where Amphan was at its best intensity. This indicates the fact that intensity of the cyclone drives dominant oceanic response (Lin, 2012). This study also brings forward the regional differences in the responses of the ocean to the forcing of cyclone. For example, observations from Argo suggested that both entrainment and upwelling contributed to the surface cooling at that location. At the location of the moored buoy in the northern BoB, however, upwelling was observed as absent and wind induced mixing results in entrainment alone. At this location the vertical entrainment can be considered as driver of ocean cooling, whereas in the central Bay at the location of Argo, vertical entrainment and upwelling can be considered as the drivers of ocean cooling. This shows that the relative position of the oceanic features to the cyclone track determines the response of the ocean to the cyclone.

One of the key findings of this study is the intense cooling ($\sim$4°C) in the cold wake which spanned all over the BoB. Vertical entrainment and upwelling contributed to the strong cooling observed, but in different regions of the BoB the contributions from these were different. Many previous researchers conducted experiments to assess the impact of cyclones on the oceans. Though significant progress has been made in understanding the oceanic processes under cyclones, there is a continuous need to identify the processes and mechanisms which induce the oceanic response due to cyclones. It should be noted that each cyclone is different and as it passes over oceanic regions of different conditions, the resulting responses of the ocean also will be different.

5. Conclusions

This study used synergistic observations from satellite and in-situ to understand the oceanic responses to super-cyclone Amphan during 16—20 May in the year 2020. Various parameters such as sea surface temperature, sea surface salinity, surface currents, surface chlorophyll concentration, subsurface temperature, salinity and currents are assessed. Spatial analysis using AMSR-2 data show significant sea surface temperature cooling in the wake of Amphan with a cooling amplitude reaching up to of $\sim$4°C. Not only a rightward bias in sea surface temperature cooling, but a large spatial extent of the cooling spanning entire BoB is observed. Surface salinity increased to the right of the track ($>$1.5 PSU) and slightly decreased along the left of the track. The strong asymmetric rain rate towards the left side of the cyclone track of amplitude $\sim$6 mm/hr is attributed to the suppressed salinity wake along the left side of the cyclone track. While the intense freshwater influx due to the cyclone rains freshened the water on the left, strong vertical mixing induced by the winds of the cyclone resulted in the influx of saltier water and increase in the salinity on the right of the track. Similarly, there is an enhancement of $\sim$1.5 mg m^{-3} of surface chlorophyll concentration after the passage of the cyclone, which is centred along the track of the cyclone where the cyclone winds were the highest. The surface chlorophyll and sea surface temperature variability are observed as collocated and tightly coupled to each other suggesting the common causal factors are the same. Surface and subsurface currents observed revealed that currents are strongly modulated by the passage of Amphan. It is observed that spatially, the sea surface temperature, salinity and surface currents exhibited rightward biases which is due to the rotation of the wind vector with the wind-driven inertial currents.

The vertical structure of the ocean is also clearly affected by the passage of cyclone in addition to the changes in the surface layer. Subsurface observations showed that Amphan induced strong subsurface mixing occurred vertically in the upper 150 m of the water column. The OHC estimated from the Argo observations revealed heat lost during the cyclone in the upper 150 m depth. Mixed layer heat and salinity budget estimations showed that the vertical mixing was the dominant process driving the mixed layer salinity and temperature response during Amphan. Vertical mixing induced by the super-cyclone brought cooler and saltier waters from below which resulted in the cooling and increase of salinity in the near surface layers. Observations from Argo revealed that the mixed layer depth was deepened, and the thermocline depth shoaled, both were the manifestations of the entrainment and upwelling induced by the cyclone. However, at the moored buoy location, upwelling was absent and entrainment was the major factor driving the variability of salinity and temperature. It is seen that regional

differences in the response of ocean were observed due to Amphan. More details into the spatially distinct oceanic response can be deciphered with the availability of more in-situ datasets. This study also reports the recovery time of all the parameters considered. Studies on the recovery of the parameters after passage of cyclones are limited. It is observed that upper ocean recovered in approximate 2 weeks after the passage of Amphan.

It is concluded that the synergistic use of in-situ and satellite observations are required to understand the complete picture of the upper ocean response to tropical cyclones. Understanding the response of the oceans to cyclones is important in the recent times when the frequency and intensity of tropical cyclones are observed to have increased. As the tropical cyclone activity increases, an increase in the oceanic response also could be expected. The present study points that while in-situ observations are relatively sparse, an extended network of the same is vital for better understanding the variability of the ocean during cyclones.

Declaration of competing interest

The authors declare that they have no known competing financial interests or personal relationships that could have appeared to influence the work reported in this paper.

Acknowledgement

Argo data (DOI: https://doi.org/10.25921/q97e-d719) were collected and made freely available by the International Argo Program and the national programs that contribute to it (http://www.argo.ucsd.edu, http://argo.jcommops.org). The Argo Program is part of the Global Ocean Observing System. GSFC — NASA are sincerely acknowledged for making available the level-3 chlorophyll data pertaining to VIIRS. We express our sincere gratitude to all concerned who has directly or indirectly contributed for the successful execution of this project. This research did not receive any specific grant from funding agencies in the public, commercial, or not-for-profit sectors. We greatly acknowledge Indian National Centre for Ocean Information Services (ESSO-INCOIS) for providing the moored buoy data. We thank the two anonymous reviewers for their valuable comments and suggestions which helped in improving this manuscript immensely.

References

Babin, S.M., Carton, J.A., Dickey, T.D., Wiggert, J.D., 2004. Satellite evidence of hurricane-induced phytoplankton blooms in an oceanic desert. J. Geophys. Res. 109, C03043. https://doi.org/10.1029/2003JC001938

Behera, S.K., Deo, A.A., Salvekar, P.S., 1998. Investigation of mixed layer response to Bay of Bengal cyclone using a simple ocean model. Meteorol. Atmos. Phys. 65, 77—91. https://doi.org/10.1007/BF01030270

Bender, M.A., Ginis, I., Kurihara, Y., 1993. Numerical simulations of tropical cyclone—ocean interaction with a highresolution coupled model. J. Geophys. Res. 98, 23245. https://doi.org/10.1029/93JD02370

Black, P.G., 1983. Ocean temperature changes induced by tropical cyclones. The Pennsylvania State University, 278 pp.

Black, W.J, Dickey, T.D., 2008. Observations and analyses of upper ocean responses to tropical storms and hurricanes in the vicinity of Bermuda. J. Geophys. Res. Oceans. 113, C08009. https://doi.org/10.1029/2007JC004358

Burpee, R.W., Black, M.L., 1989. Temporal and spatial variations of rainfall near the centers of two tropical cyclones. Mon. Weather Rev. 117, 2204—2218.

Chacko, N., Ravichandran, M., Rao, R.R., Shenoi, S.S.C., 2012. An anomalous cooling event observed in the Bay of Bengal during June 2009. Ocean Dynam. 62, 671—681. https://doi.org/10.1007/s10236-012-0525-9

Chacko, N., 2017. Chlorophyll bloom in response to tropical cyclone Hudhud in the BoB: Bio-Argo subsurface observations. Deep Sea Res. Pt. I. 124, 66—72. https://doi.org/10.1016/j.dsr.2017.04.010

Chacko, N., 2018. Insights into the haline variability induced by cyclone Vardah in the BoB using SMAP salinity observations. Remote Sens. Let. 9 (12), 1205—1213. https://doi.org/10.1080/2150704X.2018.1519271

Chacko, N., 2019. Differential chlorophyll blooms induced by tropical cyclones and their relation to cyclone characteristics and ocean pre-conditions in the Indian Ocean. J. Earth Syst. Sci. 128, 177. https://doi.org/10.1007/s12040-019-1207-5

Chen, C.T.A., Liu, C.T., Chuang, W.S., Yang, Y.J., Shiah, F.K., Tang, T.Y., Chung, S.W., 2003. Enhanced buoyancy and hence upwelling of subsurface Kuroshio waters after a typhoon in the southern East China Sea. J. Marine Syst. 42, 65—79.

Chen, L.S., Li, Y., Cheng, Z.Q., 2010. An overview of research and forecasting on rainfall associated with landfalling tropical cyclones. Adv. Atmos. Sci. 27, 967—976.

Cheung, H.F., Pan, J., Gu, Y., Wang, Z., 2013. Remote sensing observation of ocean responses to Typhoon Lupit in the northwest Pacific. Int. J. Remote Sens. 34, 1478—1491.

Chu, P.C., Veneziano, J.M., Fan, C., 2000. Response of the South China Sea to tropical cyclone Ernie 1996. J. Geophys. Res. 105 (C6), 3991—14009.

Cione, J.J., Uhlhorn, E.W., 2003. Sea surface temperature variability in hurricanes: Implications with respect to intensity change. Mon. Weather Rev. 131, 1783—1796.

Corbosiero, K.L., Molinari, J., 2003. The relationship between storm motion, vertical wind shear, and convective asymmetries in tropical cyclones. J. Atmos. Sci. 60, 366—376.

Dare, R.A., McBrie, A., 2011. Sea Surface Temperature Response to Tropical Cyclones. Mon. Weather Rev. 139 (12), 3798—3808. https://doi.org/10.1175/MWR-D-10-05019.1

D'Asaro, E.A., Sanford, T.B., Niiler, P.P., Terrill, E.J., 2007. Cold wake of Hurricane Frances. Geophys. Res. Lett. 34, L15609. https://doi.org/10.1029/2007GL030160

Du, J., Park, K., 2019. Estuarine salinity recovery from an extreme precipitation event: Hurricane Harvey in Galveston Bay. Sci. Total Environ. 670, 1049—1059. https://doi.org/10.1016/j.scitotenv.2019.03.265

Gierach, M.M., Subrahmanyam, B., 2008. Biophysical responses of the upper ocean to major Gulf of Mexico hurricanes in 2005. J. Geophys. Res. 113, C04029. https://doi.org/10.1029/2007JC004419

Girishkumar, M.S., Suprit, K., Jayaram, C., Udaya Bhaskar, T.V.S., Ravichandran, M., Shesu, V., Rama Rao, E.P, 2014. Observed oceanic response to tropical cyclone Jal from a moored buoy in the south-western Bay of Bengal. Ocean Dynam. 64, 325—335. https://doi.org/10.1007/s10236-014-0689-6

Jayaram, C., Udaya Bhaskar, T.V.S., Kumar, J.P., Swain, D., 2019. Cyclone enhanced chlorophyll in the BoB as evidenced from satellite and BGC-Argo float observations. J. Indian

Soc. Remote Sens. 47, 1875–1882. https://doi.org/10.1007/s12524-019-01034-1

Joseph, J.K., Balchand, A.N., Hareeshkumar, P.V., Rajish, G., 2007. Inertial oscillation forced by the September 1997 cyclone in the Bay of Bengal. Current Sci. 92 (2007), 790–794.

Kara, A.B., Rochford, P.A., Hurlbutt, H.E., 2000. Mixed layer depth variability and barrier layer formation over the North Pacific Ocean. J. Geophys. Res. 105 (C7), 16783–16801.

Lin, I.-I., Liu, W.T., Wu, C.-C., Wong, G.T.F., Hu, C., Chen, Z., Liang, W.-D., Yang, Y., Liu, K.-K., 2003. New evidence for enhanced ocean primary production triggered by tropical cyclone. Geophys. Res. Lett. 30, 1718.

Lin, I.I., 2012. Typhoon induced phytoplankton blooms and primary productivity increase in the western North Pacific subtropical ocean. J. Geophys. Res. 117, C03039. https://doi.org/10.1029/2011JC007626

Mandal, S., Sil, S., Shee, A., Swain, D., Pandey, P.C., 2018. Comparative analysis of SCATSAT-1 gridded winds with Buoys, ASCAT, and ECMWF winds in the Bay of Bengal. IEEE J. Sel. Top. Appl. 11 (3), 845–851. https://doi.org/10.1109/JSTARS.2018.2798621

Maneesha, K., Murty, V.S.N., Ravichandran, M., Lee, T., Yu, W., McPhaden, M.J., 2012. Upper Ocean Variability in the BoB during the Tropical Cyclones Nargis and Laila. Prog. Oceanogr. 106, 49–61. https://doi.org/10.1016/j.pocean.2012.06.006

McPhaden, M.J., Meyers, G., Ando, K., Masumuto, Y., Murty, V.S.N., Ravichandran, M., Syamsudin, F., Vialard, J., Yu, L., Yu, W., 2009. RAMA: The Research Moored Array for African–Asian–Australian Monsoon Analysis and Prediction. B. Am. Meterol. Soc. 459–480. https://doi.org/10.1175/2008BAMS2608.1

Navaneeth, K.N., Martin, M.V., Joseph, K.J., Venkatesan, R., 2019. Contrasting the upper ocean response to two intense cyclones in the Bay of Bengal. Deep-Sea Res. Pt. I. https://doi.org/10.1016/j.dsr.2019.03.010

Paulson, C.A., Simpson, J.J., 1977. Irradiance measurements in the upper ocean. J. Phys. Oceanogr. 7, 952–956.

Prakash, K.R., Panth, V., 2017. Upper oceanic response to tropical cyclone Phailin in the Bay of Bengal using a coupled atmospheric-ocean model. Ocean Dyn. 67, 51–64. https://doi.org/10.1007/s10236-016-1020-5

Price, J.F., 1981. Upper ocean response to a hurricane. J. Phys. Oceanogr. 11, 153–175. https://doi.org/10.1175/1520-0485(1981)011<0153:UORTAH>2.0.CO;2

Price, J.F., Sanford, T.B., Forristall, G.Z., 1994. Forced stage response to a moving hurricane. J. Phys. Oceanogr. 24, 233–260.

Qiu, W., Ren, F., Wu, L., Chen, L., Ding, C., 2019. Characteristics of tropical cyclone extreme precipitation and its preliminary causes in Southeast China. Meteorol. Atmos. Phys. 131, 613–626. https://doi.org/10.1007/s00703-018-0594-5

Rao, R.R., Sivakumar, R., 2000. Seasonal variability of the near-surface thermal structure and heat budget of the mixed layer of the tropical Indian Ocean from a new global ocean temperature climatology. J. Geophys. Res. 105, 995–1015. https://doi.org/10.1029/1999JC900220.

Reul, N., Chapron, B., Grodsky, S.A., Guimbard, S., Kudryavtsev, V., Foltz, G.R., Balaguru, K., 2021. Satellite observations of the sea surface salinity response to tropical cyclones. Geophys. Res. Lett. 48, e2020GL091478. https://doi.org/10.1029/2020GL091478

Schade, L.R., Emanuel, K.A., 1999. The ocean's effect on the intensity of tropical cyclones: Results from a simple coupled atmosphere–ocean model. J. Atmos. Sci. 56, 642–651.

Shang, S.L., Li, L., Sun, F.Q., Wu, J.Y., Hu, C.M., Chen, D.W., Ning, X.R., Qiu, Y., Zhang, C.Y., Shang, S.P., 2001. Changes of temperature and bio-optical properties in the South China Sea in response to Typhoon Lingling. Geophys. Res. Lett. 35, L10602.

Singh, O.P., Khan, T.A., Rahman, M.S., 2000. Changes in the frequency of tropical cyclones over the North Indian Ocean. Meteorol. Atmos. Phys. 75 (1–2), 11–20.

Singh, V.K., Koll, R.M. 2020. A review of the ocean-atmosphere interactions during tropical cyclones in the north Indian Ocean. https://arxiv.org/abs/2012.04384

Song, D., Xiang, L., Guo, L., Li, B., 2020. Estimating Typhoon-Induced Sea Surface Cooling Based upon Satellite Observations. Water 12, 3060. https://doi.org/10.3390/w12113060

Subrahmanyam, B., Rao, K.H., Rao, N.S., Murty, V.S.N., Sharp, R.J., 2002. Influence of a tropical cyclone on Chlorophyll-a Concentration in the Arabian Sea. Geophys. Res. Lett. 29 (22), 2065. https://doi.org/10.1029/2002GL015892

Sun, L., Yang, Y., Xian, T., Lu, Z., Fu, Y., 2010. Strong enhancement of chlorophyll a concentration by a weak typhoon. Mar. Ecol. Prog. Ser. 404, 39–50. https://doi.org/10.3354/meps08477

Sun, J., Vecchi, G., Soden, B., 2021. Sea Surface Salinity Response to Tropical Cyclones Based on Satellite Observations. Remote Sens. 13 (3), 420. https://doi.org/10.3390/rs13030420

Walker, N.D., Leben, R.R., Balasubramanian, S., 2005. Hurricane-forced upwelling and chlorophyll a enhancement within cold-core cyclones in the Gulf of Mexico. Geophys. Res. Lett. 32, L18610. https://doi.org/10.1029/2005GL023716

Yue, X., Zhang, B., Liu, G., Li, X., Zhang, H., He, Y., 2018. Upper Ocean Response to Typhoon Kalmaegi and Sarika in the South China Sea from Multiple-Satellite Observations and Numerical Simulations. Remote Sens. 10, 348. https://doi.org/10.3390/rs10020348

Zhang, H., Xiaohui, L., Renhao, W., Chen, D., Dongna, Z., Xiaodong, S., Yuan, W., Xunshu, S., Weifang, J., Linghui, Y., Yongfeng, Q., Di, T., Wenyan, Z., 2020. Sea Surface current response patterns to tropical cyclones. J. Marine Syst. 208, 103345. https://doi.org/10.1016/j.jmarsys.2020.103345